

A MODULAR DESCRIPTION OF THE GEOMETRY IN MONTE CARLO MODELING STUDIES FOR NUCLEAR MEDICINE

D. BOLLINI, R. CAMPANINI, N. LANCONELLI*, and A. RICCARDI

*Department of Physics, University of Bologna, and INFN Bologna
Viale B. Pichat 6/2, 40127 Bologna, Italy*

**nico.lanconelli@bo.infn.it*

M. GOMBIA

*Lab. of Montecuccolino - DIENCA, University of Bologna
Via dei Colli 16, 40136 Bologna, Italy
INFN - Bologna, Viale B. Pichat 6/2, 40127 Bologna, Italy*

Received 1 November 2001

Revised 14 December 2001

EGS is a very popular Monte Carlo code, used in the simulation of Nuclear Medicine devices. Simulation techniques are particularly effective to optimize collimator configuration and camera design in Single Photon Emission studies. With the EGS code, users must define the geometry where particles are transported. This can be both a very hard task and a source of inefficiency, especially in the case of complex geometries as, for instance, hexagonal hole collimators or pixellated detectors. In this paper we present a modular description of such geometries. Our method allows the computation of the region a point belongs to in a few steps; thus we are able to calculate this region in a reduced number of operations, independently of the collimator and detector dimensions. With a modular description we can reduce the computational time by 30%, with respect to a “traditional” description of the geometry. We validated the modular description in the simulation of a Nuclear Medicine apparatus for scintimammography. Two different collimators have been considered: one with square holes and one with hexagonal holes. We accomplished their characterization and tested their performance in a torso–breast phantom. Outcomes of the two collimators are comparable, even if it seems that the hexagonal hole collimator, thanks to its greater septal penetration, could give slightly better results for small tumors located near the collimator.

Keywords: Monte Carlo; Nuclear Medicine; EGS; Modular Geometry; SPECT.

1. Introduction

The use of Monte Carlo simulation techniques is widespread in the development of Nuclear Medicine apparatus.^{1,2} They are particularly useful when experimental measurements are impractical or to answer questions, which cannot be addressed by experimental investigations (e.g., “which fraction of photons have scattered?”),

“which is the effect of X-ray fluorescence?”). Monte Carlo methods offer a possibility of gaining an understanding of the physics that forms images and provide help in developing procedures to improve these images. Simulations can also be helpful in the choice of the camera design in SPECT (Single Photon Emission Computed Tomography) studies³: parameters such as collimator configuration and detector pixel size are often first optimized by means of simulated data and then experimentally tested.

The most widely used tool for primary breast cancer screening is X-ray mammography, which has high diagnostic value in detecting breast lesions, but often cannot be used to differentiate reliably between benign and malignant abnormalities. In addition, sensitivity of mammography in patients with dense breasts can be low. For suspect breast tumors, some studies demonstrated that scintimammography can improve the detection of carcinomas. Furthermore, thanks to its high specificity, SPEM (Single Photon Emission Mammography) based on Tc^{99m} radiotracer is very helpful in discriminating benign from malignant cases.^{4,5}

EGS is a well-known code (in its versions EGS4 and EGSnrc, the latest one),⁶ which permits the transport of photons and electrons in various media; here the user must provide a code, which describes the geometry: this is the most challenging programming aspect. Unfortunately, for complex geometries, this could be a very hard part to achieve. This is the case of one of the most common type of collimators used in SPECT: the hexagonal hole in hexagonal lattice collimator. It is indeed not easy to give an efficient and simple description of such geometry. A “traditional” way to describe regions in EGS code is to consider them as bounded by the intersection of different planes.⁷

In Monte Carlo simulation tasks the high computational time is often a drawback: realistic calculation can take several days of CPU time; hence improved calculating efficiency is desirable. Four methods have been used to reduce computational time: variance reduction techniques, physical processes approximation, efficient description of the geometry and code parallelization.^{8,9} Variance reduction techniques try to improve the efficiency by increasing the weight of useful events (in our case photons which reach the detector). Physical approximation procedures tend to neglect physical processes that are not important in the considered system. An efficient geometric description has to compute the region a point belongs to in a very few steps. Code parallelization methods exploit the inherent parallel nature of Monte Carlo history-based codes, which can be easily mapped into several processors. All these approaches can be used together, saving a larger amount of time. In this paper we present a modular description of collimators and detectors in EGS code: our procedure allows both an easy way to characterize the geometric scenario and an efficient description of the various regions. We also distribute the computational load among four processors, by means of message-passing libraries.

We validated and tested the modular description in a Nuclear Medicine study: the characterization and the comparison of the performance of two different collimators in a planar scintimammographic apparatus. Nevertheless, our procedure

retains its validity and efficiency both in other Nuclear Medicine applications (e.g., the assessment of tomographic image reconstruction techniques or the analysis of scatter correction methods) and in any cases where a collimator or a pixellated detector is involved.

2. Methods

2.1. Modular description of the geometry

Users adopting the EGS code must perform themselves a couple of tasks: the description of the regions, which constitute the geometry of the apparatus and the scoring of outputs. The most difficult section is often, when giving a point with coordinates (x, y, z) , the computation of the region the point belongs to. This is particularly true in case of complex geometries such as hexagonal collimators. This task is crucial because it is called several times during the transport of a particle; therefore any inefficiency here is propagated through the entire transport and could dramatically increase the execution time.

In order to reduce the computational time and to give a clear description of the collimator (or detector), we characterize it in a modular way: essentially the collimator is seen as a basic cell repeated in space. Luckily the collimator can easily be described in a modular way for both square and hexagonal holes. The hexagonal cell is depicted on the left side of Fig. 1: r_hole represents the radius of the hole, $septa$ the septal thickness of the parallel collimator and $xcell$ the side of the cell. Each cell consists of six triangular regions, each subdivided into an “air” region and a “lead” region (respectively the transparent and the shadow regions in Fig. 1). By repeating the basic cell we can obtain the hexagonal 2D lattice shown in the right

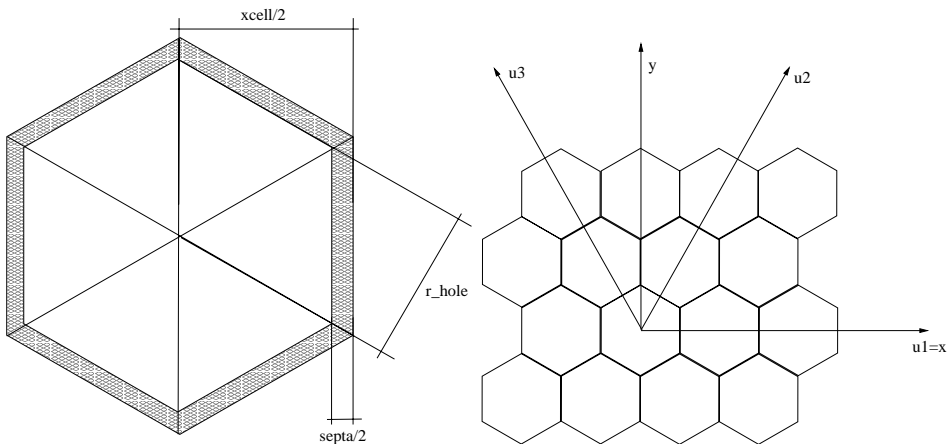


Fig. 1. Left: the basic cell, which is repeated in a modular way; r_hole is the radius of the collimator holes, $septa$ is the septal thickness and $xcell$ is the side of the cell. Right: the coordinate system chosen for the description of the 2D hexagonal lattice.

section of Fig. 1. There is also depicted the coordinate system (u_1, u_2, u_3) chosen to describe the points of the space ((x, y) is the usual Cartesian system).¹⁰

The transformation between the two systems is clearly:

$$\begin{cases} u_1 = x, \\ u_2 = \frac{1}{2}x + \frac{\sqrt{3}}{2}y, \\ u_3 = -\frac{1}{2}x + \frac{\sqrt{3}}{2}y. \end{cases}$$

In that way each triangular region, which constitutes the basic cell, is univocally determined by three indexes $(u_{1cell}, u_{2cell}, u_{3cell})$ given by:

$$\begin{cases} u_{1cell} = (int) \left(\frac{u_1}{x_{cell}/2} \right), \\ u_{2cell} = (int) \left(\frac{u_2}{x_{cell}/2} \right), \\ u_{3cell} = (int) \left(\frac{u_3}{x_{cell}/2} \right). \end{cases}$$

It is worth noting that the computation of these three operations is sufficient to calculate the location of any points of space, regardless of the number and the dimension of the holes and the septa. Another significant issue is that the only information we have to know are the collimator dimensions (width, height and length), the septal thickness and the hole radius.

2.2. Case study: Simulated apparatus

In Fig. 2 there is depicted the simulated phantom, consisting of: 3D torso (including heart), one moderate compressed breast (typical breast thickness of 6 cm) and the

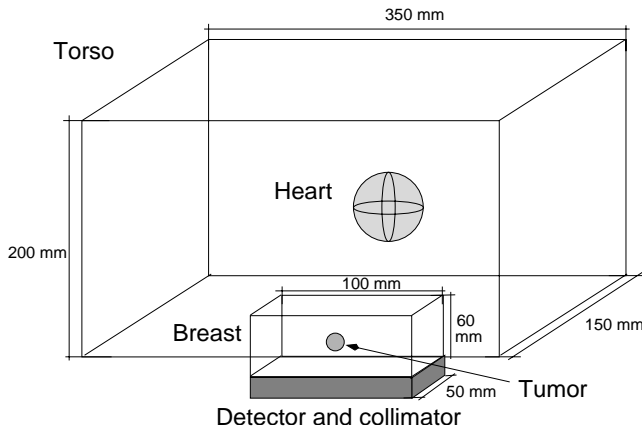


Fig. 2. Sketch of the simulated apparatus.

Table 1. Number of simulated photons for a 10 minute scintimammographic examination.

	Activity [nCi/cc]	Volume [cc]	# of photons [$\cdot 10^6$]
Torso	80	10500	16600
Heart	1600	268	8480
Breast	80	300	475
6 mm tumor	400	0.11	0.98
8 mm tumor	400	0.27	2.40
10 mm tumor	400	0.52	4.62

collimator–detector camera in cranio-caudal position. This apparatus represents a common phantom used in scintimammographic studies.³ In order to emulate a clinical examination, the number of simulated photons is calculated from an imaging time of 10 minutes and a background activity of 80 nCi/cc is assumed for the torso and the breast. Heart and tumor are characterized by a Tumor to Background (T/B) ratio of, respectively, 20:1 and 5:1, gaining a specific activity of 1600 nCi/cc and 400 nCi/cc. The number of simulated gamma rays, for that phantom and for spherical tumors of different diameter, is displayed in Table 1. We can note that a 10 minute examination consists on the emission of about 25 billions 140 keV photons (the emission energy of Tc^{99m}).

The Monte Carlo code used is EGSnrc, the latest version of EGS family. Our simulations include all the physical processes available with EGS: Compton and Rayleigh scattering, photoelectric absorption with emission of fluorescence photons or Auger electrons. In addition, we fully transport photons and electrons (the lower energy cut-off is equal to 5 keV). These assumptions hold in the entire simulated apparatus; it is worth remarking that there are no restrictions or approximations regarding physical aspects.

The simulated camera, shown in Fig. 3, consists of a lead collimator and a Ge pixellated detector, both surrounded by a lead shielding. We have considered two

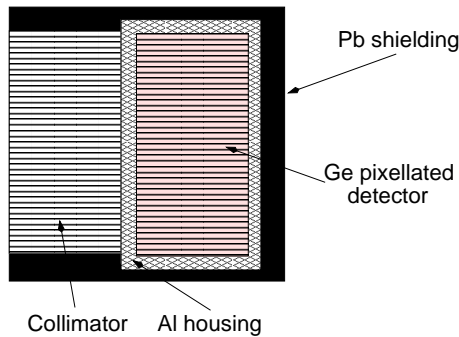


Fig. 3. The simulated camera: A lead parallel hole collimator and the pixellated detector. The lead shielding is shown in black.

Table 2. Features of the two simulated collimators.

	Square hole	Hexagonal hole
Hole diameter [mm]	1.8	1
Septa [mm]	0.2	0.2
Length [mm]	20	10
Sensitivity [counts/min/ μ Ci]	1160	1115
Spatial resolution @ 10 cm [mm]	10.8	11.0

high-sensitivity parallel hole collimators: one with square holes and one with hexagonal holes; their features are displayed in Table 2. The pixellated detector consists of an array of $2 \times 2 \times 11$ mm³ pixels incorporated in a 1.5 mm-thick Aluminum housing, as shown in Fig. 3. The detector intrinsic energy resolution is equal to 1% FWHM (Full Width at Half Maximum) at 140 keV and it is simulated by convolving the deposited energy with a Gaussian with 1% FWHM. The probability for 140 keV photons to interact in an 11 mm thick Germanium detector is about 70%, and the photopeak efficiency is equal to 67%.

3. Results

In Fig. 4 an example of the spatial distribution of photons emitted by a parallel beam source exiting from a hexagonal hole collimator is shown: this is a qualitative way to test that the geometric modular description of the collimator is correct. In

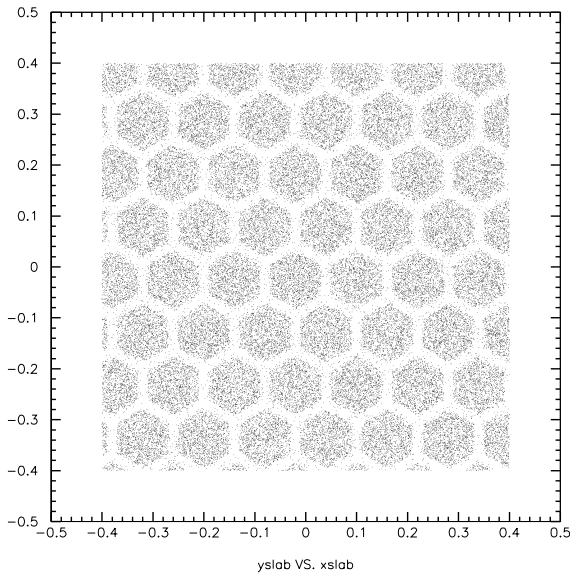


Fig. 4. Example of the spatial distribution of photons exiting from the parallel hexagonal collimator.

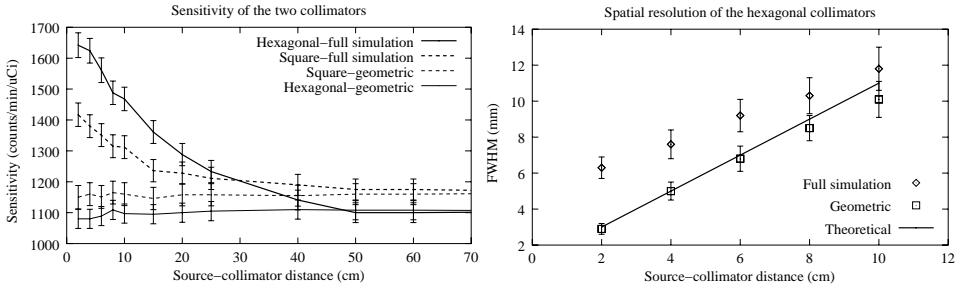


Fig. 5. Characterization of the collimators. Left: “geometric” and “full simulation” sensitivity (theoretical predictions are displayed in Table 2). Right: “full simulation”, “geometric” and theoretical spatial resolution (for a better visualization only the values obtained with the hexagonal collimator are shown).

order to validate the modular description in a quantitative way we performed the characterization of the two collimators. We calculated their sensitivity and spatial resolution and compared them with the theoretical predictions. The conditions to achieve these results are as follows: we set up two different simulations with a point source in air located at various distances from the collimator. The first simulation, called “geometric”, neglects septal penetration, scattering or any other physical effect inside the collimator (a photon is immediately discarded when it impinges on the collimator lead). The second kind of simulation, called “full simulation”, includes all the physical effects available with EGS. Sensitivity is computed as the number of photons detected per minute and μ Ci. Spatial resolution is equal to the FWHM of the collimator–detector response to the point source. Some results are depicted in Fig. 5: we can notice that the “geometric” sensitivity is in good agreement with theoretical values in the entire range of distances, whilst the “full simulation” values agree only for distances greater than 40 cm. At smaller distances we get a sensitivity greater than the theoretical one because the latter does not take into account septal penetration: at small distances the number of photons, which can reach the detector after having penetrated the collimator septa, is rather high; whereas, for photons coming from greater distances this effect is less significant for geometric reasons. Septal penetration plays an important role also in the spatial resolution of the collimators: indeed, once again, “geometric” results agree with theoretical ones, whilst “full simulation” FWHM is always greater than the theoretical prediction.

The importance of using a proper shielding, which surrounds the camera, is illustrated in Fig. 6. There are depicted two histograms of the detected events: the first without shielding and the second with a lead shielding as shown in Fig. 3. The detector response in presence of shielding is quite uniform, whereas, without shielding, peaks are present at the boundaries of the detector. This is due to the contribution of the background events, coming from torso, heart and breast.

We have also examined the optimization of acceptance energy window for minimizing background effects. With detectors made of Germanium, it is possible to

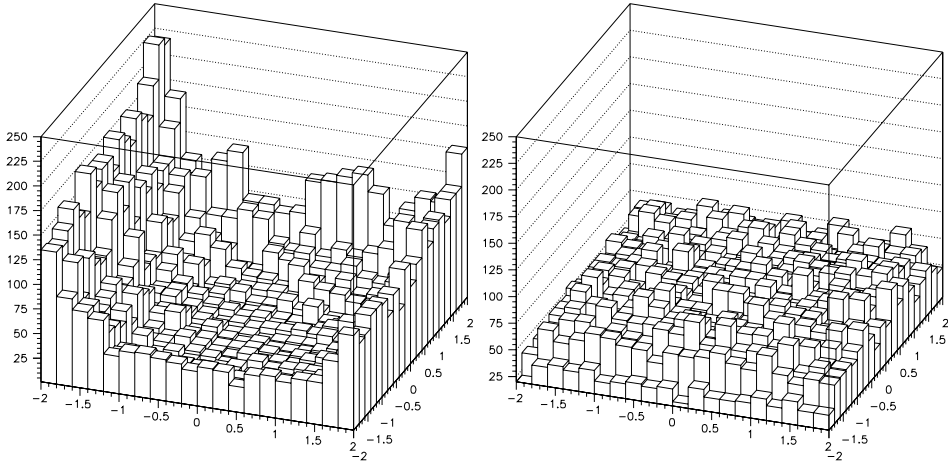


Fig. 6. Detected events for the torso–breast phantom: without shielding (left) and with lead shielding surrounding the camera (right).

Table 3. Fraction of photons detected, coming from the different parts of the torso–breast phantom (for a 8 mm tumor 1 cm deep, with $2 \times 2 \text{ mm}^2$ pixels).

Energy window	Torso	Heart	Breast	Tumor
No energy window	31%	24%	31%	14%
126–154 keV	4.5%	2.5%	52%	41%
138–143 keV	2%	1%	52%	45%

use a very narrow energy window, thanks to the excellent energy resolution of Germanium itself. Indeed, with a 138–143 keV window, the fraction of photons coming from the torso and the heart is very low (3% of the total detected photons). That value would be equal to 7%, with a typical energy window used with Anger cameras (126–154 keV) and 55%, if we consider the entire spectrum. The percentage of photons coming from the different sections of the simulated phantom are shown in Table 3, for three considered energy windows. It is worth mentioning that the contribution of the torso (including the heart) is almost entirely rejected, by using a Germanium detector.

Another issue investigated is the comparison of the performance of the two collimators in term of SNR (Signal-to-Noise Ratio), spatial resolution and contrast. To this end, we calculated these parameters for spherical tumors of different diameter located inside the breast at various depths (1 cm, 3 cm, 5 cm from the collimator front side).

SNR is defined as:

$$\text{SNR} = \frac{\sum_{\text{ROI}} \text{detected tumor events}}{\sqrt{\sum_{\text{ROI}} \text{all detected events}}}, \quad (1)$$

Table 4. Summary of the results of the simulated torso–breast phantom, for three different spherical tumors and the two considered collimators.

Tumor diameter (mm)	Tumor depth (cm)	FWHM		SNR		Contrast	
		Square (mm)	Hex. (mm)	Square	Hex.	Square %	Hex. %
6	1	6.0	6.1	6.4	7.0	20	23
6	3	7.5	7.3	3.3	3.8	10	12
6	5	9.2	10.3	2.3	2.2	4	4
8	1	6.5	7.6	11.6	12.9	43	47
8	3	7.1	8.6	7.3	8.1	15	17
8	5	9.5	10.8	4.7	4.5	9	8
10	1	7.9	8.8	19.3	19.6	45	42
10	3	9.3	9.9	13.7	13.3	30	27
10	5	10.4	11.5	8.5	8.4	15	15

where the dimension of the square ROI (Region of Interest) on which to calculate the SNR is adjusted to maximize SNR itself. Spatial resolution is defined as the FWHM of a Gaussian fit of the detected tumor events.

Contrast is defined as:

$$\text{Contrast} = \frac{\langle \text{detected tumor events} \rangle_{\text{ROI}}}{\langle \text{detected background events} \rangle_{\text{ROI}}}, \quad (2)$$

where $\langle x \rangle_{\text{ROI}}$ means the average value of x inside the same ROI used in SNR calculation. Results are summarized in Table 4 and (some of them) depicted in Fig. 7. The performance of the two collimators are generally comparable both in term of SNR and contrast and FWHM; however, it seems that the hexagonal collimator, thanks to its higher sensitivity at short distances, gives a slightly better SNR in cases when the tumor depth is not very high. This effect is more evident for small tumors (i.e., in cases of low statistics). Figure 8 displays an example of an 8 mm tumor, 1 cm deep, as seen by the simulated camera with the two different collimators. We can notice that the hexagonal collimator gives a better contrast, despite its worse spatial resolution. Hexagonal hole collimators are easily available

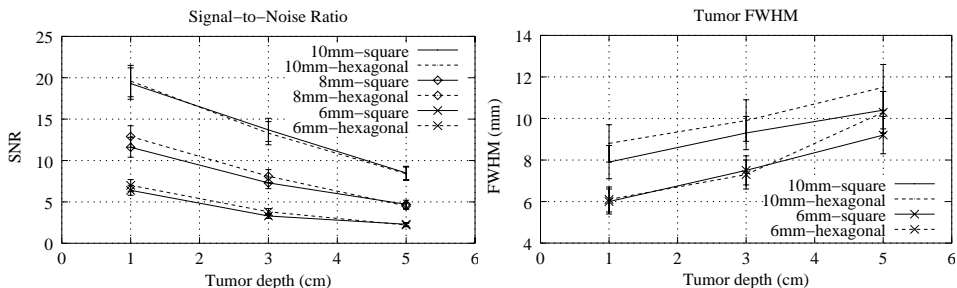


Fig. 7. Dependence of (left) tumor SNR and (right) tumor FWHM on the two collimators. For both plots spherical tumors of different diameter are considered in the simulated phantom.

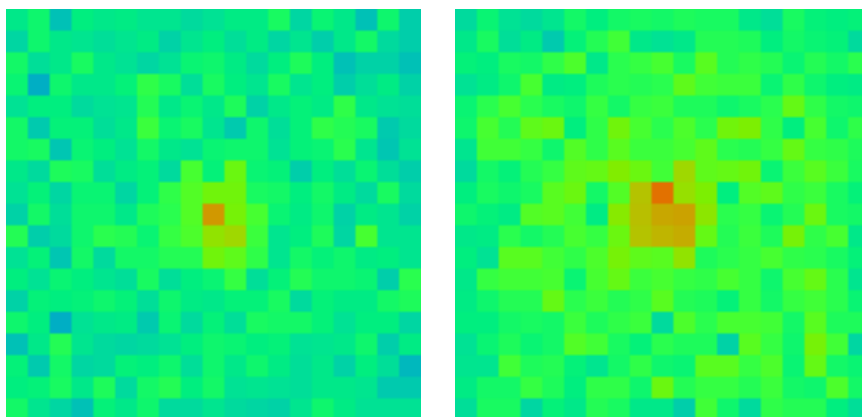


Fig. 8. Simulated images for a 8 mm diameter tumor 1 cm deep. Pixel size is 2×2 mm². Left: square hole collimator. Right: hexagonal hole collimator.

from industry and have a more symmetric septal penetration pattern than square hole collimators. On the other hand, hexagonal holes generally suffer from aliasing problems due to geometric mismatch between the collimator and square detector pixels; however, this effect is small if the hole size is less than about half the pixel size.¹¹ Therefore, we reckon that the hexagonal collimator used is more suitable for the detection of small tumors located near the collimator.

The simulation of different collimator–detector configurations for the entire torso–breast phantom can be hampered by the huge computational time required. In our study we distributed the computational load between four PIII 800 MHz processors (two dual processor machines), by means of PVM (Parallel Virtual Machine) message-passing libraries, following a master–slave paradigm. PVM assures flexibility and portability of the code, allowing the use of distributed heterogeneous resources such as cluster of PCs. In practice, the master program performs the following tasks:

- reads the input simulation data from an external file;
- sends a fraction of events to slave processes;
- receives and collects the outcomes of the detected events;
- stores the results in an external file.

Each slave accomplishes the transport of the photons assigned and sends back to the master the coordinates and the energy deposited of the detected events. Slaves are self-scheduled, asking master new events to process, as their task ends. Modular description permits the reduction of the computational time by 30%, with respect to a “traditional” geometric description.⁷ That allows the simulation of an entire torso–breast phantom for different configurations: each run takes almost 40 days of CPU time on the ensemble of four PIII 800 MHz processors. The simulation of one

run consists of about 25 billions 140 keV photons, emitted in a 10 minute acquisition clinical examination; we recall that full transport of photons and electrons is considered and all the physical effects available are used. The majority of the time (about 98%) is spent in the transport of the torso–heart photons, whereas the simulation of all the tumors considered for the performance analysis summarized in Table 4 has required less than an hour of computational time. Luckily, the simulation of the torso–heart has to be performed only once for each collimator; after that, we can simulate separately in a very short time all the tumors we are interested in. This is one of the main advantages of Monte Carlo simulations with respect to experimental measurements: experiments have to be repeated completely every time. In scintimammographic apparatus this is a critical point because it is very difficult to repeat the experiment in the same conditions, especially using phantoms based on technetiated water (the most widely phantoms used). It is indeed hard to get the same exact T/B ratio, or the same exact location, especially when small tumors are involved.

Communications between master and slaves during the calculation do not afflict the efficiency of the algorithm: the overhead due to the communication is negligible, since data transferred between master and slaves consist of only a few bytes (seed for random number generator, coordinates and energy of the detected events). Furthermore, the time spent in reading input data and writing output results is insignificant, compared to the computational time. Hence, we can affirm that the speed-up is nearly linear, by increasing the number or the frequency of the processors used. That allows a drastic reduction of the computational time, when a cluster of fast processors is available. However, the bottom line is that with our modular description we are able to decrease the computational time by 30%, independently of the number and type of the utilized processors.

4. Conclusion

In this paper we presented a geometric description for collimators and pixellated detectors in EGS code. With this method we achieve the computation of the region a point belongs to in a few steps, giving rise to a reduction in computational time by 30%, with respect to a “traditional” geometric description. Our modular description allowed the investigation of collimator properties, taking into account all the physical effects available with EGS code. In this way, we found out that septal penetration plays an important role in collimators performance, especially at small distances, where both sensitivity and FWHM response of the collimators increase their values, thank to septal penetration.

Then we compared two different collimators with equal sensitivity: one with square holes and one with hexagonal holes. We tested them in a simulation of a torso–breast phantom for scintimammography: their performance are generally comparable in term of SNR and spatial resolution. However, the hexagonal hole

collimator used, seems to give a better contrast for small tumors (diameter less than 8 mm) located near the camera, despite its worse spatial resolution.

Acknowledgments

This work is partially supported by MURST and University of Bologna. We would like to thank Dr. A. B. Brill for the development of Germanium detector and guidance in its analysis. We wish also to thank Prof. F. L. Navarria for his interest in this project.

References

1. H. Zaidi, *Med. Phys.* **26**(4), 574 (1999).
2. M. Ljungberg *et al.* (eds.), *Monte Carlo Calculations in Nuclear Medicine: Applications in Diagnostic Imaging* (IoP Publishing, Bristol, UK, 1998).
3. G. J. Gruber, W. W. Moses, and S. E. Derenzo, *IEEE Trans. Nucl. Sci.* **46**(6), 2119 (1999).
4. I. Khalkhali, J. A. Cutrone, I. G. Mena, L. E. Diggles, R. J. Venegas, H. I. Vargas, B. L. Jackson, S. Khalkhali, J. F. Moss, and S. R. Klein, *Radiology* **196**, 421 (1995).
5. H. Palmedo, A. Schomburg, F. Grunwald, P. Mallmann, D. Krebs, and H. J. Biersack, *J. Nucl. Med.* **37**, 626 (1996).
6. I. Kawrakow, *Med. Phys.* **27**(4), 485 (2000).
7. A. F. Bielajew, *National Research Council of Canada Report, PIRS-0341* (1995).
8. D. R. Haynor, R. L. Harrison, and T. K. Lewellen, *Med. Phys.* **18**, 990 (1991).
9. M. F. Smith, C. E. Floyd, Jr., and R. J. Jaszczak, *Med. Phys.* **20**, 1121 (1993).
10. W. E. Snyder, H. Qi, and W. Sander, *Proc. SPIE, the International Society for Optical Engineering* **3661**, 716 (1999).
11. G. J. Gruber, W. W. Moses, S. E. Derenzo, N. W. Wang, E. Beuville, and M. H. Ho, *IEEE Trans. Nucl. Sci.* **45**(3), 1063 (1998).